# Screen-Printed Resistive Tactile Sensor for Monitoring Tissue Interaction Forces on a Surgical Magnetic Microgripper

D. Anastasia Aubeeluck[1], Cameron Forbrigger[1], Sara Mohseni Taromsari[1], Tianhao Chen[2], Eric Diller[1,3] and Hani E. Naguib[1,2,4]

[1]Department of Mechanical and Industrial Engineering, University of Toronto, 5 King's College Road, Toronto M5S 3G8, Canada

[2]Institute of Biomedical Engineering, University of Toronto, 164 College Street, Toronto, Ontario, M5S 3G9, Canada

[3]University of Toronto Robotics Institute, University of Toronto Engineering, 55 St. George Street Toronto, Ontario, M5S 1A4, Canada

[4]Toronto Rehabilitation Institute, 550 University Ave, Toronto, Ontario, M5G 2A2, Canada

**ABSTRACT -** With the recent development of novel miniaturized magnetically-controlled microgripper surgical tools (of diameter 4 mm) for robot-assisted minimally invasive endoscopic intraventricular surgery, the surgeon loses feedback from direct physical contact with the tissue. In this case, surgeons will have to rely on tactile haptic feedback technologies to retain their ability to limit tissue trauma and its associated complications during operations. Current tactile sensors for haptic feedback cannot be integrated to the novel tools primarily due to size limitations and low force range requirements of these highly dextrous surgical operations. This study introduces the design and fabrication of a novel 9 $mm^2$, ultra-thin and flexible resistive tactile sensor whose operation is based on variation of resistivity due to changes in contact area and piezoresistive (PZT) effect of the sensor's materials and sub-components. Structural optimization was performed on the sub-components of the sensor design including microstructures, interdigitated electrodes, and conductive material in order to improve minimum detection force while maintaining low hysteresis and unwanted sensor actuation. To achieve a low-cost design suitable for disposable tools, multiple layers of the sensor sub-component were screen printed to produce thin flexible films. Multi-walled carbon nanotubes (MWCNTs) and thermoplastic polyurethane (TPU) composites were fabricated, optimized, and processed into suitable inks to produce conductive films to be assembled with printed interdigitated electrodes and microstructures. The assembled sensor's electromechanical performance indicated three distinct linear sensitivity modes within the sensing range of 0.04 - 1.3 N. Results also indicated repeatable, and low time responses while maintaining flexibility and robustness of the overall sensor. This novel ultra-thin screen-printed tactile sensor of 110 µm thickness is comparable to more expensive tactile sensors in terms of performance and can be mounted onto the magnetically-control micro-scale surgical tools to increase safety and quality of endoscopic intraventricular surgeries.

**KEYWORDS:** Robot-assisted minimally invasive surgery, multi-walled carbon nanotubes, thermoplastic polyurethane, pressure sensors, flexible electronic devices, piezoresistive, screen printing

## 1. Introduction

In the wake of robot-assisted minimally invasive surgeries (RMIS) getting more intricate and more complex with narrower workspaces for surgical operations, the integration and implementation of multiple surgical tools and robotic systems at a miniaturized scale have become increasingly pertinent. This stems from the need to improve surgical precision, dexterity, and efficiency during surgeries [1] [2]. RMIS aims to create smaller incisions in patients, reduce recovery time, lower risks of infection, shorten operating time, reduce probability of revision procedures and lower pain in patients [1] [3].

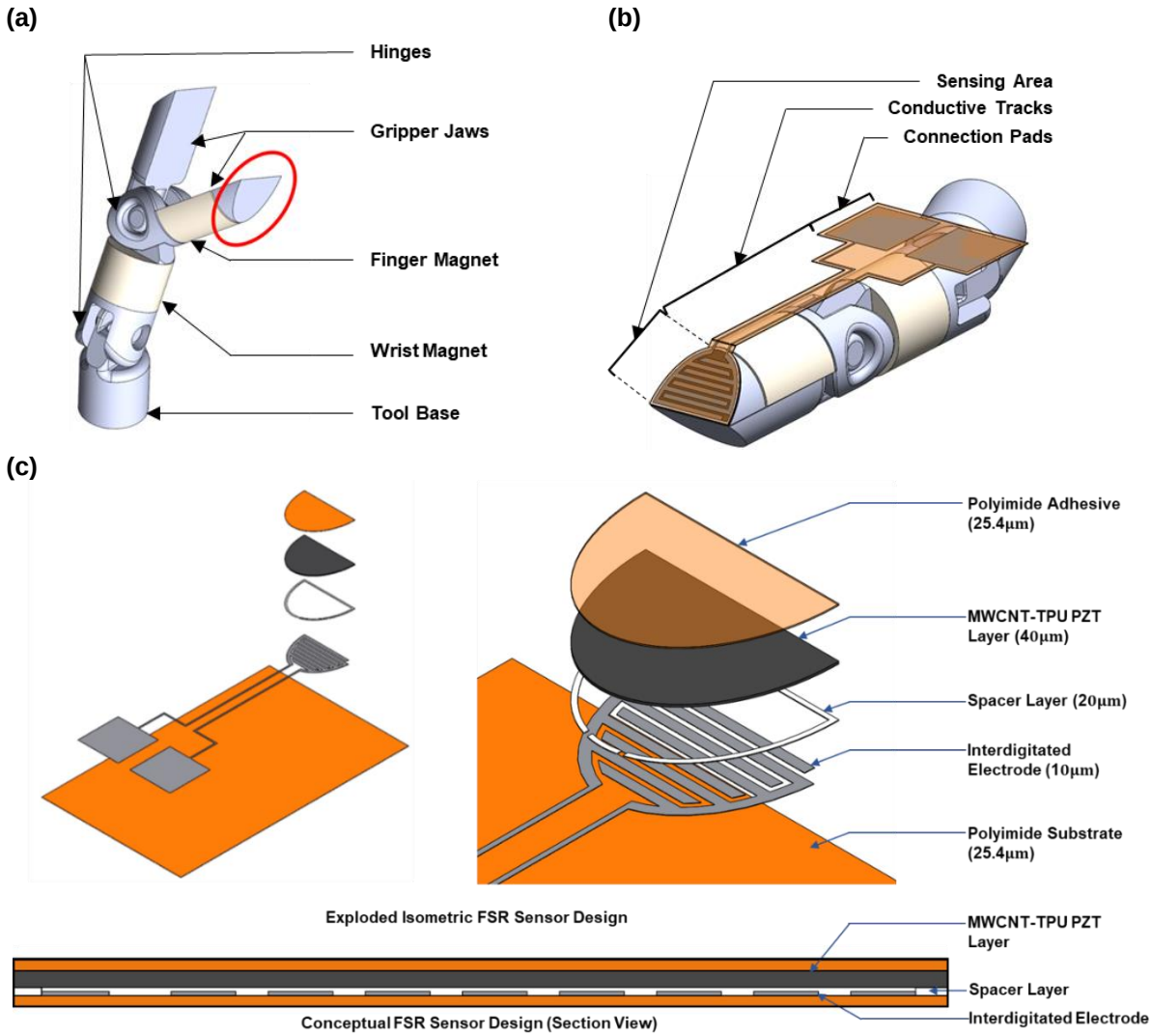


**Figure 1.** (a) CAD design of Magnetic Microgripper with a 9 $mm^2$ Surface Area of tip area. (b) CAD of 3D printed Magnetic Microgripper and resistive tactile sensor, (c) Schematic illustration of multilayered resistive tactile sensor design (FSR sensor design).

With pediatric neurosurgical operations specifically requiring even further constrained working spaces, Lim et al. and Forbrigger et al. developed miniaturized robotic surgical tools for neuroendoscopy with a novel magnetic microgripper end-effector (of diameter 4 mm as shown in Figure 1 (a)) able to fit within a millimeter-scale channel and able to operate at a neuroventricular scale using magnetic actuation and concentric tube robots (CTR) [1] [2] [4]. Owing to the working space constraint, surgeons would be unable to have direct access to tissues and organs. Hence, must rely on tactile haptic feedback technologies to restore tactile and force information to prevent loss in sensory information to decrease the risks of tissue trauma and its associated complications during minimally invasive endoscopic intraventricular surgeries [2]

[3] . For the miniaturized robotic surgical tools for neuroendoscopy with a novel magnetic microgripper end-effector, the requirement for a tactile solution involves a low force range (0 to 1.35 N), high sensitivity, low hysteresis, low response time, high accuracy, high repeatability, biocompatibility (for tools entering the body temporarily) and lastly, customized geometries for the surface of the surgical tool as per Trejos et al. and Puangmali et al. [3] [5] [6] [7] [8]. Biocompatibility involves being functional, non-toxic, and not causing any immune response during tool-tissue interactions during surgery (wet conditions) [3] [9].

Current tactile haptic feedback solutions cannot be integrated to the novel tools primarily due to bulkiness, size limitations and low force range requirements (0 to 1.35 N) of the highly dextrous surgical operations for neurosurgery [10] [6]. Furthermore, micro-scale surgical tools involve multiple types of end-effectors including grippers, scissors, graspers, and end-suction) that require different highly unique and customized thin flexible tactile sensors on its surfaces. Fabrication of current state-of-the-art and commercially available tactile sensors have been associated with lithographic technologies due to its ability to produce highly accurate and precise high-performance devices for miniaturized tactile sensors [10] [11]. However, photolithographic technologies, despite their numerous merits, involve high fabrication costs, labor-intensive processes, costly chemicals, specialized equipment and clean room facilities which adversely affect innovative development and implementation onto novel surgical tools [12] [13]. Moreover, with increasing demand for disposal surgical tools to avoid tedious and costly sterilization processes, novel magnetically-controlled surgical tools may be disposable if associated with an overall lower operational cost [14].

To overcome haptic feedback challenges for a disposable surgical magnetically-controlled microgripper, this study introduces a novel 9 $mm^2$, ultra-thin and flexible resistive tactile sensor (Sensing Area) attached to the surface of the tool as shown in Figure 1 (b). Conductive tracks and connection pads are added for ease of data acquisition for sensor characterization and their design is not investigated in this study. The resistive tactile sensor consists of a force sensing resistor (FSR) system that relies on the combination of electrical contact theory and piezoresistive (PZT) effect, where variation of an external static force stimuli causes a change in electrical resistivity [10] [11] [15]. Electrical contact theory involves the changes in geometrical surface area of the electrodes in contact with the conductive or semi-conductive material (sensing material) [16] [17]. The piezoresistive effect involves resistance changes of the conductive or semi-conductive material [16] [17]. Tactile sensors using resistance changes as their transduction principle have numerous advantages including simple construction, low cost, durability, robustness, large measurement range, and high sensitivity [11] [15] [18]. The proposed sensor study consists of investigating the structural design and the implementation of flexible sub-components to reduce hysteresis and improve sensor performance. The unique surface area of the tip of the microgripper was selected for this study to capture necessary haptic information on its surfaces in real-time as it is the first intentional or non-intentional point of contact between tool-tissue during navigation, probing and opening of the gripper jaws during RMIS operations. To lower the cost per tool device, this study applied screen printing technologies in combination with advanced material science development to fabricate thin flexible films to produce multiple layers of the sensor sub-component. Screen printing was preferred over other low-cost additive manufacturing approaches, such as 3D printing, due to its ability to accommodate a wide range of ink viscosities, its simplicity and ease of use, its faster production time, and its consistency and reproducibility of complex print patterns [19].

In this study, structural and material optimizations on the sub-components of the sensor design for spacer microstructures, interdigitated electrodes and conductive material were performed to improve minimum detection force and sensibility (ability to sense force stimuli) range while maintaining low hysteresis, unwanted sensor actuation and sensitivity. Figure 1 (c) depicts the different sub-components within the sensor structural design. Multi-walled carbon nanotubes (MWCNTs) and thermoplastic polyurethane (TPU) composites were fabricated, optimized, and processed into suitable inks to produce conductive films and piezoresistive films to be assembled with optimized designs of printed interdigitated silver electrodes. MWCNT as conductive particles were selected due to their high aspect ratio and low percolation thresholds in thermoplastics while TPU was selected due to its processability into suitable inks and good dispersion

with MWCNT particles [20] [21]. The material selection and material design for the conductive films and sensing materials were based on facile manufacturing, biocompatibility, flexibility, sheet resistivity, and piezoresistive performance which are dependent on weight percentage of conductive MWCNT within the TPU matrix. The concentration of conductive composite was tuned to increase its piezoresistive performance to enhance the overall sensitivity of the sensor. To further improve sensor performance, interdigitated silver electrodes were geometrically optimized and microstructures using silicone ink were added to the assembled sensor to strategically adjust the microscopic contact area and gap between electrode and piezoresistive material. To avoid interference with the external magnetic field actuating the magnetic surgical tool, all materials for the sensor were selected based on weak diamagnetic behaviour [22] [23] [24].

## 2. Experimental Section

### 2.1 Materials

Screen-printable silver ink (Metalon® HPS-FG32 Silver Screen Ink) supplied by NovaCentrix was chosen for conductive tracks and interdigitated electrodes. Kapton® Polyimide film, purchased from McMaster-Carr, with adhesive was used as substrate and laminating agent. Screen-printable silicone ink (125-26 (SP) A/B) supplied by Creative Materials Inc., is a two-component ink chosen for the addition of microstructures for the spacer layer in the multi-layered sensor structure. For the conductive ink, Multi-Walled Carbon Nanotubes (MWCNT - NC7000™) powder, purchased from Nanocyl, and Thermoplastic Polyurethane pellets (TPU - Pearlbond™ 12F75UV), supplied by Lubrizol Advanced Materials, were chosen as the conductive filler and the matrix, respectively. The other solvents used for conductive and piezoresistive ink formulation are N, N-dimethylformamide (DMF) and Tetrahydrofuran (THF) from Sigma Aldrich.

### 2.2 Fabrication of Sensor Sub-Components & Sensor Assembly

As depicted in Figure 1 (c), the sensor comprised of an upper polyimide adhesive, a MWCNT-TPU conductive layer, a spacer layer and an interdigitated electrode printed on a polyimide substrate. To formulate the screen-printable conductive layer, different weight percentages of MWCNT (0 wt%, 2.5 wt%, 5 wt%, 7.5 wt%, 10 wt% and 12.5 wt%) with TPU polymer loading fixed at 20 wt% to solvent content was fabricated as outlined in Figure 2 (a). THF and DMF solvents at a ratio of 2:2:1 ratio to TPU was used to disperse different weight percentages of MWCNT using ultrasonification. TPU pellets were then added to the dispersed MWCNT incrementally to allow uniform dispersion and melting. The solutions were allowed to magnetically stir at 70$^{o}$C at 500 RPM for 24 hours. The highly viscous inks were then degassed in a vacuum chamber and sealed to avoid evaporation of solvent content. To verify screen printability of the conductive inks and prior to screen printing, the MWCNT-TPU-DMF-THF ink solutions were heated to 70$^{o}$C and stirred. For screen-printable silicone ink (125-26 (SP) A/B), Part A and Part B at a ratio of 1:1 were added and manually stirred together.

Screen printing was performed using a manual 8 in. by 10 in. screen printer (Model MSP-088) along with emulsion screens (Hary Manufacturing Inc, New Jersey, USA) as shown in Figure 2(b). The patterns for the different sensor sub-component designs were prepared using AutoCAD (Autodesk, Inc., Mill Valley, CA) and implemented on stainless-steel screen printing mesh. Using a polyurethane squeegee (Hary Manufacturing Inc, New Jersey, USA) with an optimal angle of attack of 45° and ink speed of about 60-70 $mms^{-1}$, ink paste is sheared at the screen's top surface, forced through the mesh opening while the emulsion is pressed against the substrate as the squeegee is moved across the screen. The patterned material is deposited onto the substrate when the screen emulsion lifts off as the pressure from the squeegee is withdrawn [25]. Figure 2 (b) depicts the screen printing process. The conductive inks were then used to fabricate the conductive film using the aforementioned printing procedure. The design of the unique and customized sensing area of 9 $mm^2$ based the surface of the surgical tool was prepared using AutoCAD and then patterned onto screen frames. Screen-printable conductive inks with varying MWCNT concentrations were screen printed with a single print stroke onto polyimide substrate using the patterned screen frames and air dried in a fume hood. This process was repeated 5 times until a 5 layered MWCNT-TPU composite on polyimide substrate was obtained.

To fabricate the interdigitated electrodes prints, various designs with constant spacing of 100 µm and varying electrode width (50 µm, 100 µm, 150 µm and 200 µm) with constant 100 µm conductive tracks, were prepared via AutoCAD and implemented onto patterned screen frames for screen printing. The designs were then screen printed with a single print stroke using the silver ink and patterned screen frames onto polyimide substrate and cured at 175°C for 5 minutes in an oven.

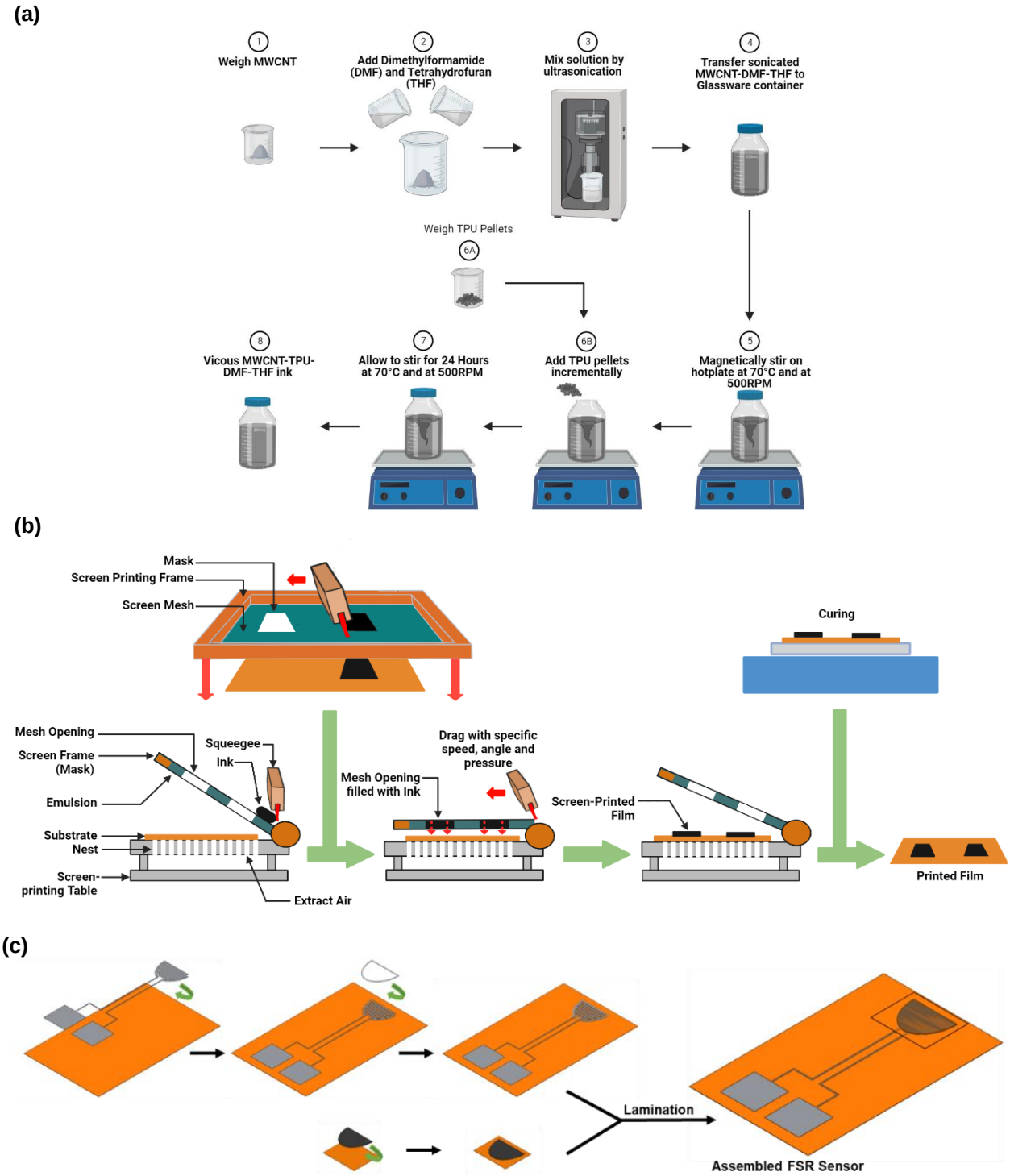


**Figure 2.** Schematic illustration for (a) fabrication process of MWCNT-TPU (conductive) ink, (b) screen printing process, (c) fabrication and assembly of resistive tactile sensor.

The design of the microstructures for the spacer layer with varying widths of 100 µm and 200 µm was prepared using AutoCAD and then patterned onto screen frames. The microstructures were screen printed onto electrode patterned substrate with a single print stroke for a deposition of 10 µm layer of silicone material. The printed microstructures were then cured at 175°C for 5 minutes in an oven. The number of layers were controlled by the number of deposition rounds.

To assemble the sensor, screen-printed interdigitated electrodes film with or without screen-printed microstructures were superimposed and aligned with screen-printed conductive film with the sensing material facing towards the silver electrodes. Subsequently, the superimposed sub-components were flattened together with a heavy roller to reduce the physical gap between the layers and to maintain uniform thickness. The flattened layers were then sealed and laminated using polyimide adhesive to insulate the conductive tracks, protect the sensor from humidity (irrigation and body fluids during surgery), and maintain the structural integrity of the multiple layers together as shown in Figure 2 (c). The roller was applied during the process to promote adhesion and eliminate any air bubbles present in the construction. Finally, the sensor assembly was cut and trimmed to size with a Disco DAD3220 Automatic Dicing Saw for better accuracy and smoother edges [26].

### 2.3 Characterization

The viscosity behavior of the formulated conductive inks was characterized using an Anton Paar rheometer (MCR 702 MultiDrive, shear rates between 0.1-100 $s^{-1}$, 25$^{o}$C) to verify the shear thinning and the printable viscosity range. Viscoelastic behavior of the inks was also analysed through amplitude sweeps to reflect dynamic conditions and determine the linear viscoelastic (LVE) range for liquid-like behavior [27] [28]. Furthermore, to simulate the screen printing process, a time-dependent controlled-shear-rate test (step test) was performed to simulate the ink at rest, during spreading and the recovery.

The analysis of the surface and cross-section morphologies of the screen-printed patterns of interdigitated electrodes, silicone microstructures and conductive film were performed using a scanning electron microscope (SEM – JSM-IT100, JEOL Corporation), after the samples were gold-sputtered. The printed integrity was also confirmed using an optical microscope in case of any ink bleeding or short circuits prior to sensor assembly.

To evaluate and identify the conductivity of MWCNT-TPU, fabricated conductive inks at different MWCNT loading were dried and cut into 2 mm diameter disk shapes. Conductivity characterization was performed using a Dielectric analyser (Alpha-N High Resolution Dielectric Analyser, Novocontrol Technologies) with a frequency sweep range of 0.1 Hz-0.3MHz. To identify percolation behavior, the conductivity at the lowest frequency (0.1 Hz) was used.

For surface resistance, printed MWCNT-TPU at varying MWCNT loading was assembled with interdigitated electrodes and were connected in series with a fixed resistor of 1 MΩ (comparable low resistance to conductive films) in a voltage divider electrical setup, powered with a constant 5 V supply. Voltage signal readings at the node between sensor and resistor ($V_{DAQ}$) was acquired in real-time via a data acquisition instrument, NIDAQ (National Instrument 6210-USB Analog DAQ box), at a sampling rate of 2000 Hz and analyzed using MATLAB R2021b software (MathWorks, Natick, MA, USA), as shown in Figure 3 (a) [26]. The readings were used to calculate and graph the surface resistance (non-actuated resistance of sensors without spacer microstructures) of printed MWCNT-TPU composite.

To evaluate the electromechanical performance of the assembled sensors, the sensors were subjected to compression tests using a universal tester (Instron 5848 Microtester) while the sensors' signals were acquired using the Sensor-Computer interface in real-time. To mimic tool-tissue interaction during neurosurgeries with brain tissue (shore hardness 4.5 ± 1.5 Shore 00), a silicone rubber tip from EcoflexTM 00-10 (Smooth-On Inc., East Texas, PA) of shore hardness of 10 Shore 00 was fashioned and attached to the end of a 3D printed cylindrical tool [26] [29] [30]. The 3D printed cylindrical tool was then clamped to the gripper of the universal tester while the assembled sensor was fixed such that the silicone tip applies

force perpendicular to the sensor. Piezoresistivity and sensor performance was characterized using the setup.

Sensitivity ($S$) for the resistive sensor and semiconductor was calculated as per the following equation:

$$S = \frac{\Delta V}{\Delta F}$$

where $\Delta V$ is the change in voltage with applied change in force, $\Delta F$, on the sensor. In this study, force and pressure applied on the sensor are used interchangeably since force and pressure are directly proportional and the force is applied uniformly across the small sensing area of tactile sensor customized for the surface of the tip of the surgical tool.

Using the Sensor-Computer interface in Figure 3 (a), the electrical integrity of the conductive tracks of the interdigitated electrodes was verified using detected signal to ensure complete circuitry. Furthermore, the physical robustness and flexibility tests were also performed by physical crumbing and flexural tests to assess the physical integrity of the assembled resistive tactile sensor.

**(a)**

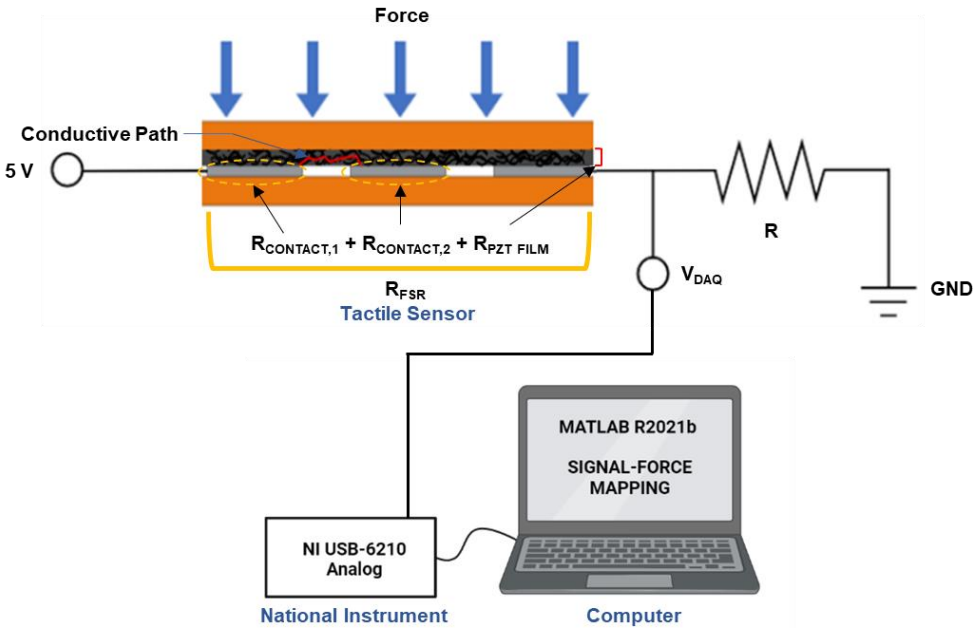


**Figure 3.** (a) Force sensing resistor (FSR) circuitry with Sensor-Computer Interface connection during characterization performance of resistive tactile sensor.

## 3. Results and Discussion

### 3.1 Conductive Ink and Film Characterization

Rheological characterization of the fluid conductive inks' results in Figure 4 (a), (b) and (c) demonstrated that all the different concentrations of MWCNT-TPU ink were screen printable despite slow recovery rate for fluid inks of lower MWCNT concentrations. Once rheological properties were validated for screen printing compatibility, the conductive inks were screen printed onto polyimide substrate. The printing of the conductive ink indicated that the solvents DMF and THF exhibited rapid evaporation and minimal clogging of the screen mesh while maintaining screen printability of the inks and reusability of the screen mesh [31]. Figure 4 (d) shows the SEM of the surface morphology of screen-printed conductive films. No significant micropores or voids were identified from the evaporation of the DMF and THF solvent on the surface. Moreover, with increasing concentration of MWCNT from 0 wt% to 12.5 wt% in MWCNT-TPU, it is observed that the surface becomes more nodular. It is speculated that this could be due to the MWCNT microfibers balling up into nodules with increasing concentration. As per Mehrad et al. and Li et al., the presence of

MWCNT particles within the TPU matrix improves the electrical conductivity of the composite by formation of direct conductive paths between the network of MWCNT particles within the TPU polymer [21] [32].

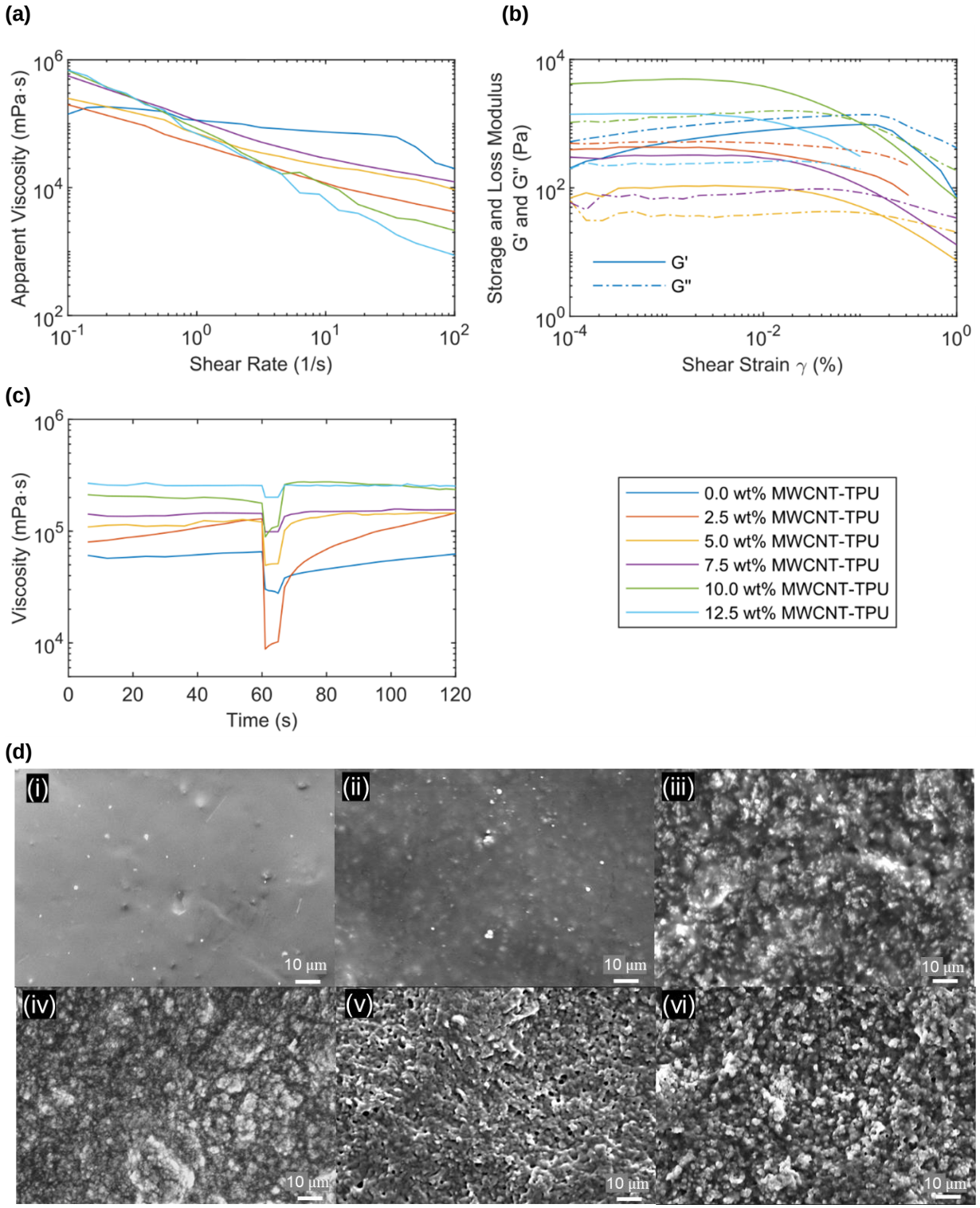


**Figure 4.** (a) Flow curve, (b) Amplitude sweep and (c) Step Test for rheology characterization of MWCNT-TPU ink, (d) Surface SEM (x1000) and Photograph Image of (i) 0 wt% MWCNT-TPU, (ii) 2.5 wt% MWCNT-TPU, (iii) 5 wt% MWCNT-TPU, (iv) 7.5 wt% MWCNT-TPU, (v) 10 wt% MWCNT-TPU and (vi) 12.5 wt% MWCNT-TPU.

## 3.2 Piezoresistive Film Optimization

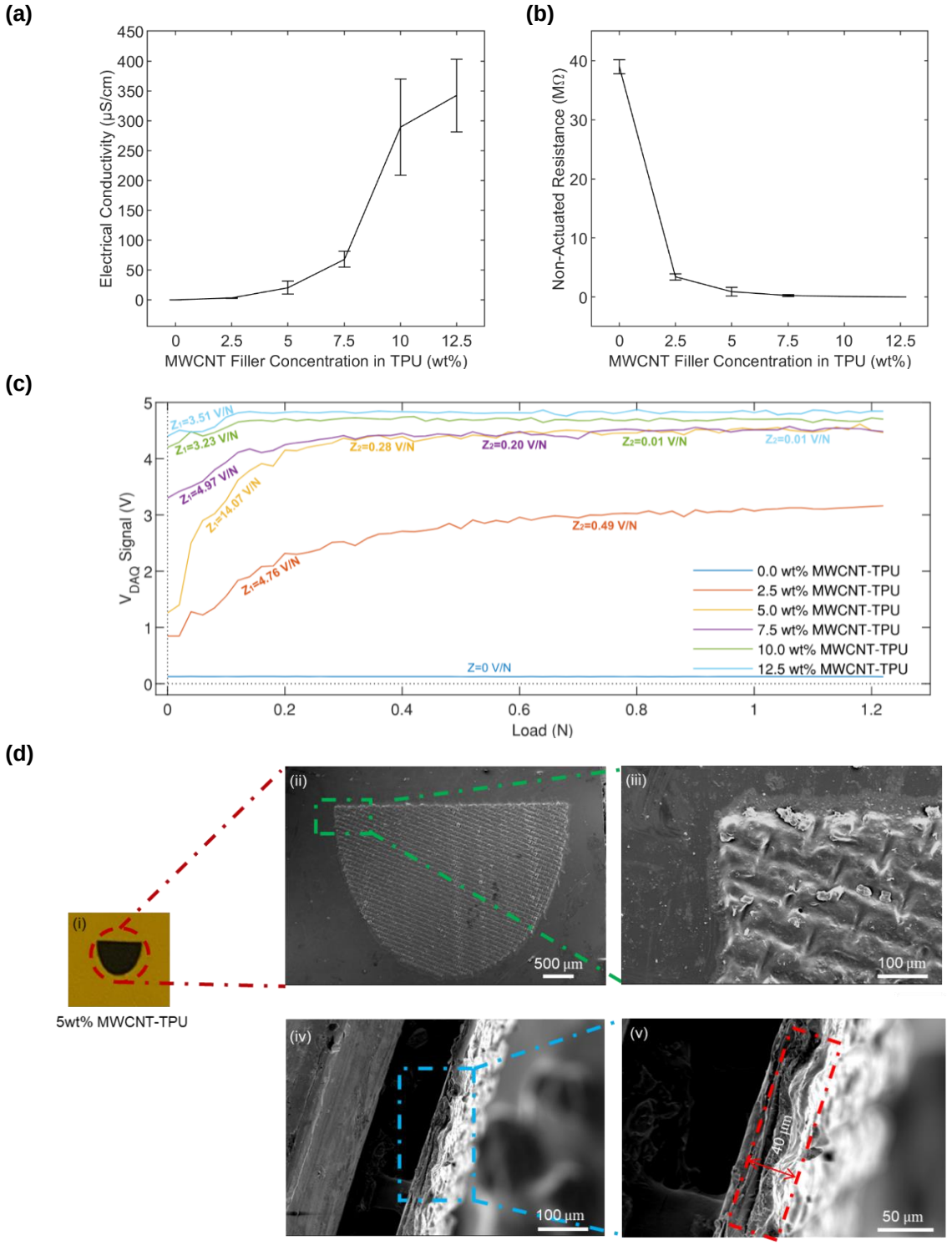


**Figure 5.** Characterization of conductive film and performance of assembled sensor with conductive film (no spacer). (a) Variation in electrical conductivity of MWCNT-TPU composite using different concentrations at 0.1 Hz, (b) Variation of electrical surface resistance of screen-printed MWCNT-TPU using different concentrations, (c) Voltage response at $V_{DAQ}$ to static loading, (d) Characteristics of 5 wt% MWCNT-TPU composite printed on polyimide substrate (i) Photograph image, (ii) SEM of surface x25, (iii) SEM of surface x200, (iv) SEM of cross-section x200, (v) SEM of cross-section x500.

Based on the conductivity results and non-actuated resistance of MWCNT-TPU film from Figure 5 (a) and 5 (b), it can be deduced that the percolation transition occurs in the range of 5 wt% MWCNT-TPU filler in TPU composite whereby the conductive filler's concentration approaches the percolation threshold [33]. This study indicates an apparent higher percolation threshold in the range of 5 wt% as critical MWCNT filler content to form conductive network compared to literature reports indicating lower percolation thresholds between 1 wt% to 4 wt% MWCNT content [34] [35]. The difference in percolation threshold could be linked to fabrication process and dispersion of MWCNT content in the TPU matrix.

To investigate the piezoresistive performance of the screen-printed MWCNT-TPU composite at different filler contents, the conductive films were assembled with interdigitated electrodes of constant dimensions (200 µm electrode widths and 100 µm spacing) and without spacer microstructures to promote maximum contact with intend to isolate the piezoresistive effect of the conductive film. The assembled conductive film and interdigitated electrodes were connected in a voltage divider electrical setup and subjected to compressive loadings while the voltage across the known resistor was acquired in real-time. This setup for testing and optimizing piezoresistivity of the conductive films was chosen to keep the geometries, construction and testing as controlled variables for consistency in performance for the final optimized sensor design. Figure 5 (c) shows the voltage change ($V_{DAQ}$ signal) due to the influence of compressive loads on the assembled sensor with different MWCNT loading in elastic TPU matrix. The magnitude of the piezoresistive effect can be determined in terms of sensitivity of the sensors which is calculated by the slope of the curve (fractional voltage change with change in load). Two almost distinct linear force ranges were identified with sensitivity modes associated with deformation of the sensor in two folds; firstly, increased contact with the electrodes surfaces due to structural deformation of the sensor assembly ($Z_1$) by small forces and secondly due to elastic deformation (z-direction) of the MWCNT-TPU film ($Z_2$) by large forces which may be attributed to the piezoresistive effect [36]. The sensitivities and the corresponding sensing ranges of different MWCNT loading in TPU matrix are summarized on Figure 5 (c). With the highest sensitivity and sensing ranges ($Z_1$ = 14.07 V/N for 0 - 0.3 N and $Z_2$ = 0.28 V/N for 0.3 - 1.3 N), the 5 wt% MWCNT-TPU sensor supports the conductivity and surface resistance results from Figure 5 (a) and (b) indicating a percolation threshold with MWCNT filler concentration near the range of 5 wt% in TPU matrix. Thus, 5 wt% MWCNT-TPU was the film chosen as the optimum candidate for the PZT sensing material of the FSR sensor.

SEMs of the surface morphology of screen-printed 5 wt% MWCNT-TPU in Figure 5 (d) indicated grid-like microfeatures and high density of MWCNT particles on the surface. The grid-like microfeatures were due to the pattern of the screen printing mesh, the high viscosity of the ink and low curing time. The SEM of the cross-section of the screen-printed PZT film indicated a thickness of 40 ± 4 µm for 5 printed layers of MWCNT-TPU composite on polyimide substrate. With a grid-like structure, the multilayered composite can deform within the grid spacings in the assembly until it is fully compressed in the z-direction. Upon application of large compressive forces, the conductive film is compressed, bringing the conductive microfibres even closer together and resulting in more conductive pathways thereby improving sensibility and sensitivity. Furthermore, the high density of MWCNT particles influenced the conductivity and piezoresistivity of the composite via quantum tunnelling and percolation [37]. The surface resistance of 5 layered screen-printed 5 wt% MWCNT-TPU film indicated good fabrication reproducibility with base resistance in the range of 1.4 MΩ and 0.5 MΩ (average 0.9 MΩ).

### 3.3 Interdigitated Electrode Optimization

A constant 100 µm spacing between each electrode finger was maintained through each electrode design for spatial resolution within the confined sensing area of 9 $mm^2$ to ensure sensitivity in the low force range. Furthermore, the electrode area was constrained not to exceed 70% of the sensing area and consequently electrode widths larger than 200 µm were not investigated. Figure 6 (a) shows the SEM of screen-printed interdigitated electrodes patterns with a constant 100 µm electrode spacing and varying electrode width of 50, 100, 150 and 200 µm. Screen-printed 200 µm interdigitated electrode patterns resulted in the best print quality with less than 1% margin of error for both electrode spacing and electrode width while the print

quality for 50 µm interdigitated electrodes pattern resulted in a margin of error of 17%. This indicated the line width limitation in terms of screen printing resolution and consequently electrode width designs less than 50 µm were not fabricated. With a low margin of error for print quality, screen printing was demonstrated to be able to fabricate intricate circuitry for interdigitated electrode designs of line width of 50-200 µm as per Figure 6 (a).

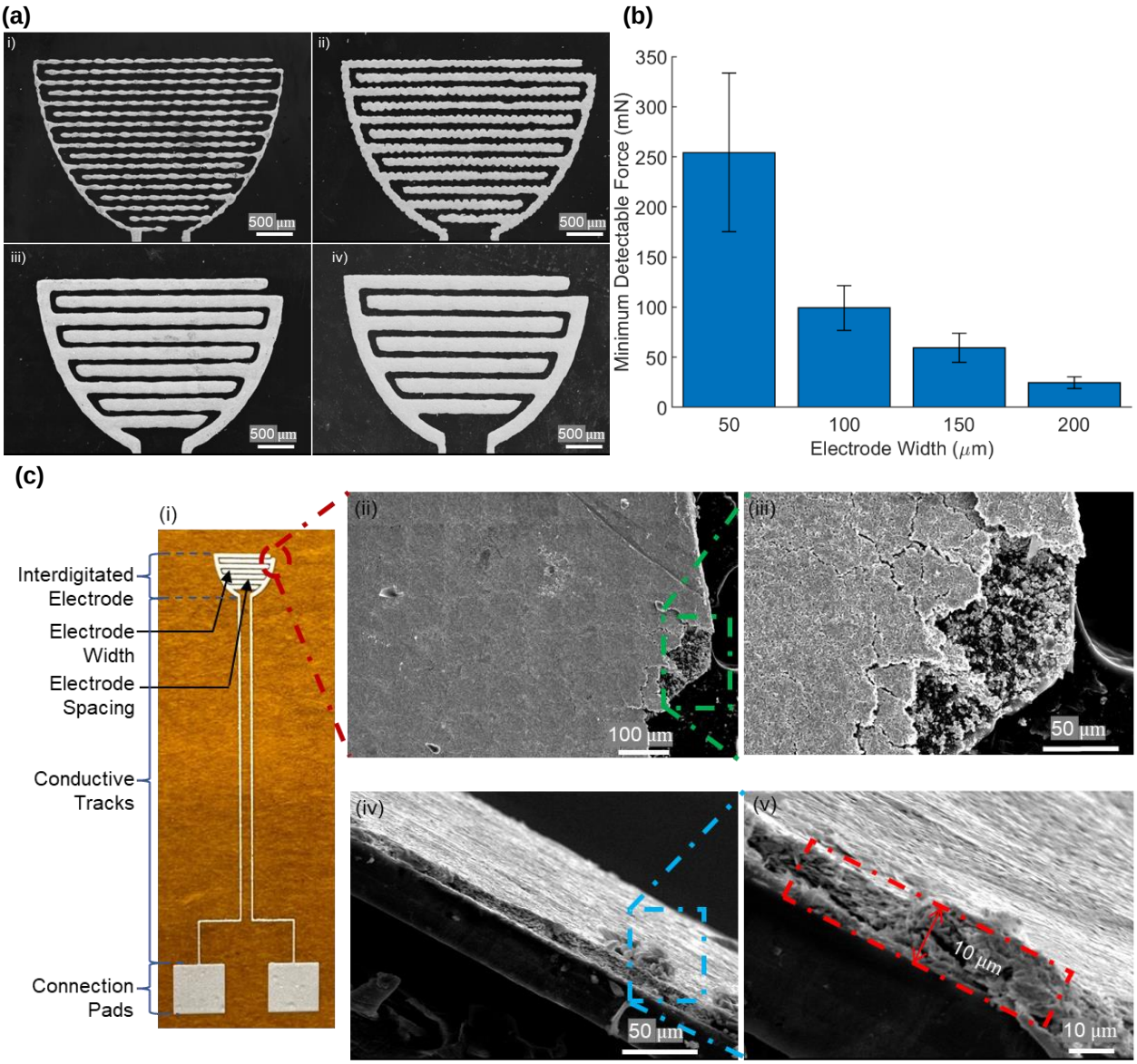


**Figure 6.** (a) Design of Interdigitated electrodes: SEM of surface (x30 magnification) of design of interdigitated electrodes of varying width of i) 50 µm, ii) 100 µm, iii) 150 µm and iv) 200 µm with a constant spacing of 100 µm , (b) Sensibility Optimization of interdigitated electrodes pattern: Minimum detectable force by sensors of varying electrode width and constant electrode spacing of 100 µm under screen-printed 5 wt% MWCNT-TPU conductive film with no spacer microstructure, (c) Characteristics of printed film (i) Photograph image of electrode layer printed on polyimide substrate, (ii) SEM of surface x160, (iii) SEM of surface x500, (iv) SEM of cross-section x500, (v) SEM of cross-section x1500.

Figure 6 (c) shows the overall electrode layer with interdigitated pattern, conductive track and connection pads printed on polyimide substrate. The printed electrode layer was verified for electrical and structural integrity prior to any assembly in case of any defects incurred during the manual printing process. Silver

ink (AgNPs) was selected for the patterned electrode layer because of its diamagnetic behavior, high conductivity, anti-oxidation properties and stability at ambient temperatures as per literature [22] [38]. These properties ensured that the sealed printed electrode's electrical integrity is maintained in the assembled sensor for consistent results for a long period of time during use and testing on the surgical magnetic tool. From Figure 6 (c), it can be clearly observed that the surface of printed electrode films is uniform, and no presence of pores were observed from the evaporation of the ink solvent. Furthermore, the printed electrode layer surface is seen without any traces of segregation or discontinuity. This indicated excellent wetting and thixotropic behavior of the silver ink. The cross-sectional SEM in Figure 6 (c) also confirms this observation. The cross-sectional SEM also indicated the electrode layer has an average thickness of 10 ± 2 μm for the application of a single print stroke.

Based on the response and recorded data from Figure 6 (b) with no spacer microstructures, it was found that wider electrode fingers (increased electrode contact surface area) allowed for lower force detection which is ideal and critical for intraventricular neurosurgical operations [39]. The interdigidated electrode pattern with electrode width of 50 μm showed the least sensibility with a minimum force of 254 ± 79 mN detected. The high standard deviation can be associated to the poor screen print quality at 50 μm line width. The lowest minimum detectable force of 24.6 ± 5.9 mN was detected by sensors with 200 μm electrode width. Due to fabrication constraints and to maintain the spatial resolution within the sensing area, the interdigitated electrodes design could not be further optimized and, thus, the 200 μm electrode width with 100 μm electrode spacing interdigitated electrode pattern was selected as a compromise for sensibility and sensitivity of the overall sensor.

### 3.4 Spacer Microstructure Optimization

Spacer microstructure of suitable size and height are identified to be added to the sensor design firstly to prevent unwanted actuation of the piezoresistive layer, secondly to ensure a low minimum detectable force and thirdly to improve the sensitivity of the overall sensor. Owing to size and fabrication limitations, the spacer design consisted of adding microstructures strategically around the interdigitated electrodes as shown in Figure 7 (a) (i), (ii) and (iii). Figure 7 (b) shows a loss in sensibility with increased spacer width from a minimum detectable force of 24.6 ± 5.9 mN for no microstructure to a minimum detectable force of 107.5 ± 10.7 mN for a spacer of 200 μm width and 10 μm height. This loss in sensibility can be explained by a decrease in contact between the interdigitated electrodes and the piezoresistive layer. 100 μm is chosen as the optimized spacer width with a minimum detectable force of 29.7 ± 2.9 mN since it reduced unwanted actuation of the overall FSR sensor while retaining a low minimum force detectable with a low standard deviation. However, the 100 μm width and 10 μm height spacer embedded within the overall sensor produced a non-zero voltage baseline and hence, the spacer height was further optimized.

To introduce a zero voltage baseline of the overall sensor, reduce further unwanted actuation and improve sensitivity, a spacer with constant 100 μm width was studied with varying height. When adding spacers between the interdigitated electrodes and the piezoresistive layer, there is an introduction of an air gap between the two layers. This air gap results in the elimination of direct conductive pathways which increases the resistance of the FSR sensor [40]. Furthermore, with increasing spacer heights, there is more resistance to create direct conduct pathways and hence, an increase in sensitivity when force is applied to deform the flexible silicone material of the spacers between the electrode layer and the piezoresistive layer. Thanks to the elastic potential of the silicone spacers, the structure of the spacers is restored quickly during unloading thereby reducing hysteresis [40]. Figure 7 (c) shows that raising spacer height increases minimum detectable force and introduces a zero voltage baseline of the sensor. 0 μm and 10 μm have low minimum detectable force but with a non-zero baseline due to contacts between electrode and piezoresistive layer under no load (no actuation). This makes them less favourable candidates. 20 μm and 30 μm spacer height produced zero voltage baseline of the sensor. Based on the sensibility results, a zero voltage baseline and low force range requirements for micro neurosurgery, 20 μm height and 100 μm width were, thus, chosen as the optimized spacer geometries for the overall FSR sensor with a minimum detectable force of 49.4 ± 6.4 mN [39] [5].

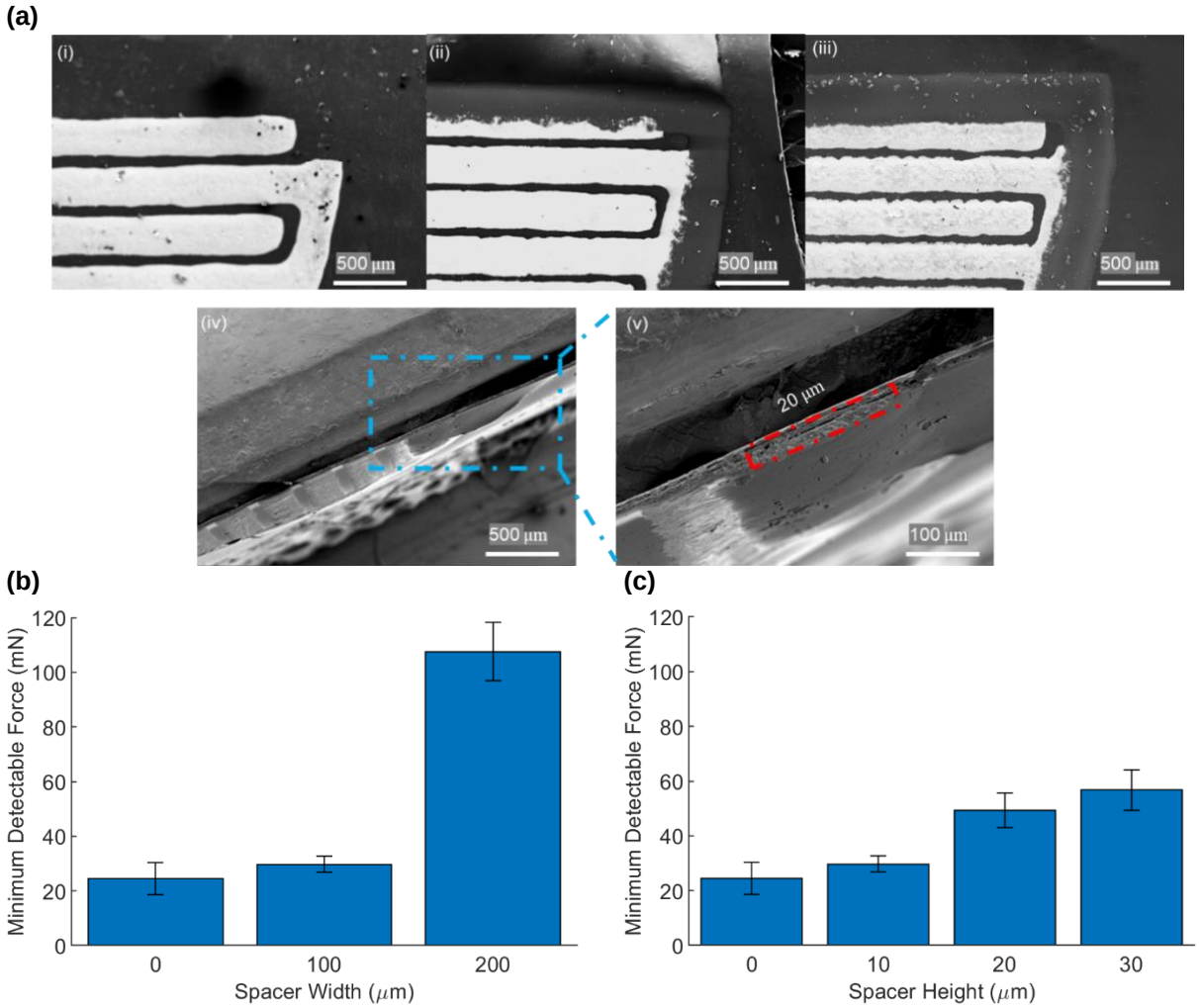


**Figure 7.** (a) Design of Spacer Microstructure: SEM of surface (x50 magnification) of spacer microstructure of varying width of i) 0 µm, ii) 100 µm and iii) 200 µm with interdigitated electrodes of 200 µm and constant electrode spacing of 100 µm. iv) SEM of cross-section x50 and v) SEM of cross-section x200 of spacer microstructure prints (2 strokes) on polyimide substrate, (b) Sensibility Optimization of spacer microstructure width design: Minimum detectable force by sensors with interdigitated electrodes of 200 µm and electrode spacing of 100 µm under screen-printed 5 wt% MWCNT-TPU conductive film with varying spacer width microstructure for one print stroke, c) Sensibility Optimization of spacer microstructure height: Minimum detectable force by sensors with interdigitated electrodes of 200 µm and electrode spacing of 100 µm under screen-printed 5 wt% MWCNT-TPU conductive film with 100 µm spacer width and varying spacer height microstructure.

### 3.5 Assembled Sensor and Working Mechanism

Using the optimized sub-components, the multiple layers of the sensor were assembled as per the fabrication and assembly process outline in section 2.2. An overall sensor of 110 ± 6 µm (n = 10) thickness with a 9 $mm^2$ sensing area was obtained as shown in Figure 8 (a) to meet the surface and physical requirements of being mounted onto the magnetically-controlled microgripper to increase safety and quality of endoscopic intraventricular surgeries. The slight variance in thickness of overall sensor between devices will affect the contact resistance effect which can in turn offset the non-actuated resistance of the sensor and the actuation of the sensor upon external tactile contact. To minimize discrepancies, the devices will have to be calibrated before use once the force-signal relationship is established. Furthermore, the sealed sensor ensures that the sensor's sensing area's sub-components are not in direct contact with tissues and bodily fluids during surgery thus, maintaining biocompatibility and functionality of the overall sensor.

The working mechanism of the multilayered resistive tactile sensor was hypothesized to be divided into three sensitivity modes. These sensitivities were defined as $S_1$ in the ultra-small force range, $S_2$ in the small force range and $S_3$ in the large force range as speculated on Figure 8 (b). Upon application of ultra-small forces, the structure of polyimide and the PZT film deform into the air gap spacing with the PZT surface coming into contact with the interdigitated electrodes (without the PZT film deforming) for a large resistance change within a narrow force range. With increasing force application (small force range), the silicone microstructure spacers deform thereby increasing the surface contact between the PZT layer and the interdigitated electrodes further. For increasingly large forces, the PZT layer deforms gradually causing segregated networks of MWCNT particles in the composite to come closer and closer together to form more conductive pathways through the material for very small resistance changes until the sensor can no longer deforms.

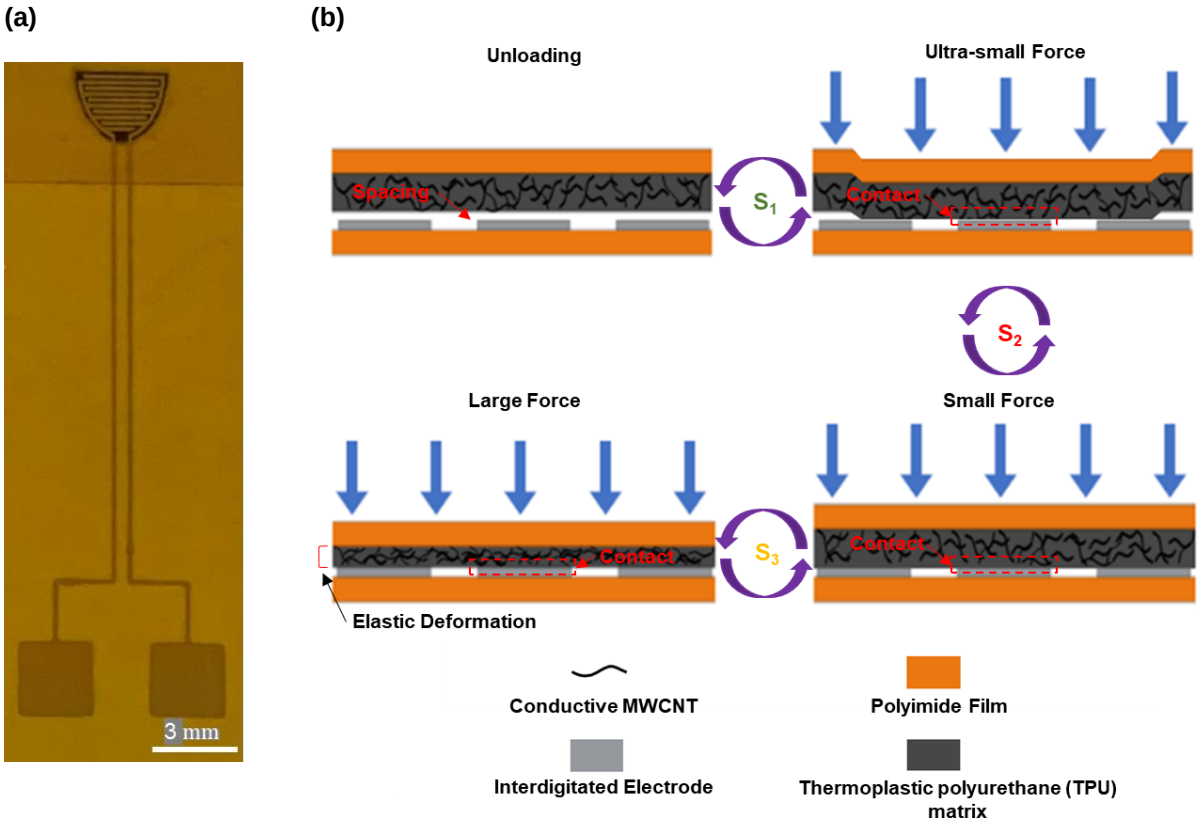


**Figure 8.** (a) Photograph of assembled resistive tactile sensor, (b) Schematic illustration of resistive transduction method and working mechanism of resistive tactile sensor.

With increasing contact between the piezoresistive layer and the interdigitated electrodes and the MWCNT particles within the piezoresistive layer coming closer, the resistance of the overall sensor decreases due to the formation of more conductive pathways with the overall sensor. This decreases the resistance of the sensor and consequently increases the voltage signal acquired across the resistor at $V_{DAQ}$ which can be used for Signal-Force mapping. Upon unloading, the sensor's silicone microstructures and piezoresistive layer regain their initial shapes thereby decreasing contact with the interdigitated electrodes, the MWCNT particles getting further apart within the composite and the destruction of conductive pathways. This increases the resistance of the FSR sensor and hence, decreases the voltage across the resistor at $V_{DAQ}$.

### 3.6 Sensor Electromechanical Performance

Using the Sensor-Computer interface setup and the universal tester, the assembled resistive tactile sensor was subjected to cyclic compression tests to characterize the sensor performance. The performance of the proposed sensor design is summarised in Table 1.

A. Time Response

To determine the time response, resistive tactile sensors (n = 10) were subjected to a loading frequency of 0.065 N/s for 5 cycles. The peaks of the reference force (1.3 N) and that of $V_{DAQ}$ signal (with a filter) were compared and superimposed as shown in Figure 9 (a). The delay, t, between the peak of the reference force and the $V_{DAQ}$ signal was used to determine the sensor time response and a calculated value of 70 ± 51 ms was obtained. The result of the proposed resistive tactile sensor is comparable to the time response of flexible piezoresistive in literature which ranges from 10 to 200 ms [41]. The high response time can be associated to delays and recovery due to the high interfacial surface adhesion between the interdigitated electrodes and the piezoresistive MWCNT-TPU film when in contact with each other [42]. Furthermore, the standard deviation of the time response is large due to the random distribution of conductive particles (MWCNT) within the PZT layer and consequently a large variation from sensor to sensor was obtained. The time response of the proposed sensor is adequate for RMIS haptic feedback systems since time delays of less than 200 ms went unnoticed to surgeons during surgeries as per literature [7]. However, the proposed sensor is well above the human tactile response time of 15 ms and, thus, still has room for improvement [43].

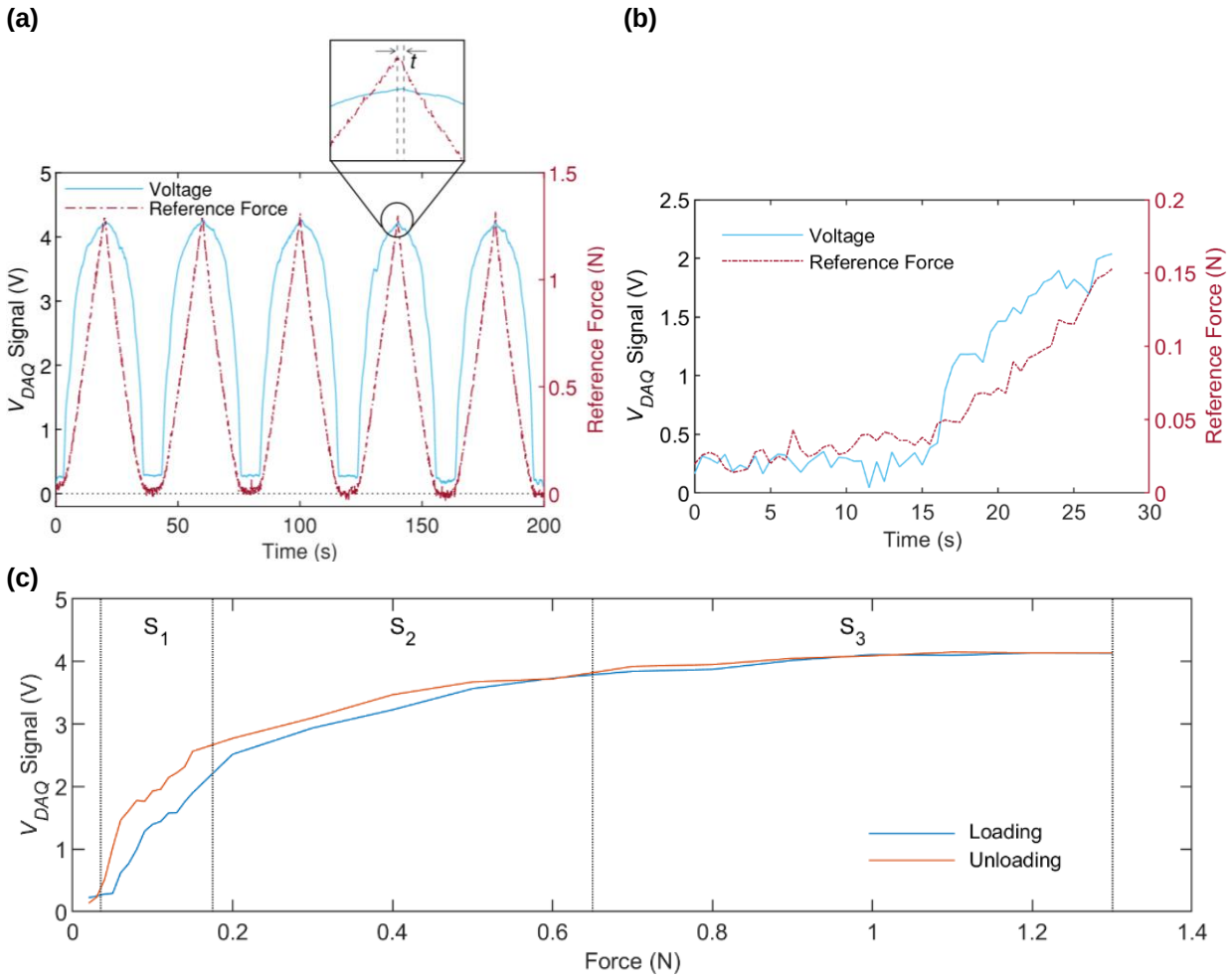


**Figure 9.** (a) Voltage ($V_{DAQ}$ signal) response of the assembled resistive tactile sensor under forces ranging from 0 to 1.3 N at a loading frequency of 0.065 N/s, (b) Voltage ($V_{DAQ}$ signal) response of the assembled resistive tactile sensor under ultra-small force ranges, (c) Sensor signal-force relationship between 0.04 and 1.30 N forces for loading and unloading.

B. Range

Using acquired $V_{DAQ}$ signal superimposed with the stimuli reference force at a loading frequency of 0.013 N/s, the minimum detectable force by the proposed sensor was determined using Figure 9 (b). The sudden rise in $V_{DAQ}$ signal by the proposed sensor at 16 s indicated a detection of the reference force which was determined as the minimum detectable force with a value of 49.4 ± 6.4 mN. To further characterize the range, the acquired $V_{DAQ}$ signal was mapped to the reference force stimuli subjected to the sensor's sensing area as shown in Figure 9 (c). A maximum force of 1.30 N was detected as $V_{DAQ}$ signal reached its peak and maximum. The overall sensible range of the proposed sensor, 0.04 - 1.30 N, is acceptable for minimally invasive endoscopic intraventricular surgeries to reduce risks of tissue trauma since it overlaps with the iatrogenic injury range for brain tissues which is between 0.49 - 0.88 N [5]. The sensible range also overlaps with the working range of dissection, coagulation, and division forces during neurosurgery with peak forces reaching 1.35 N and 70% of surgical tasks within the range of 0 to 0.3 N [6]. Moreover, Figure 9 (c) indicates three linear working ranges for the sensor; $S_1$, $S_2$ and $S_3$. $S_1$ indicates a range of 0.04 - 0.15 N for ultra-small forces, $S_2$ indicates a range of 0.15 - 0.6 N for small forces and $S_3$ indicates a range of 0.6 - 1.3 N for large forces.

C. Sensitivity and Hysteresis

Using the lowest loading frequency of 0.013 N/s for 5 cyclic loadings of resistive tactile sensors (n = 10), the sensor signal-force relationship was established to analyse the characteristics of the sensor responses. Linear fitting curves for the three working ranges were used to analyse and model the relationship between the applied stimuli forces and the $V_{DAQ}$ signal (sensor signal). To ensure the quality of linearity, the correlation coefficient $R^2$ was ensured to exceed 0.85 when characterizing the linear ranges using linear fitting curves.

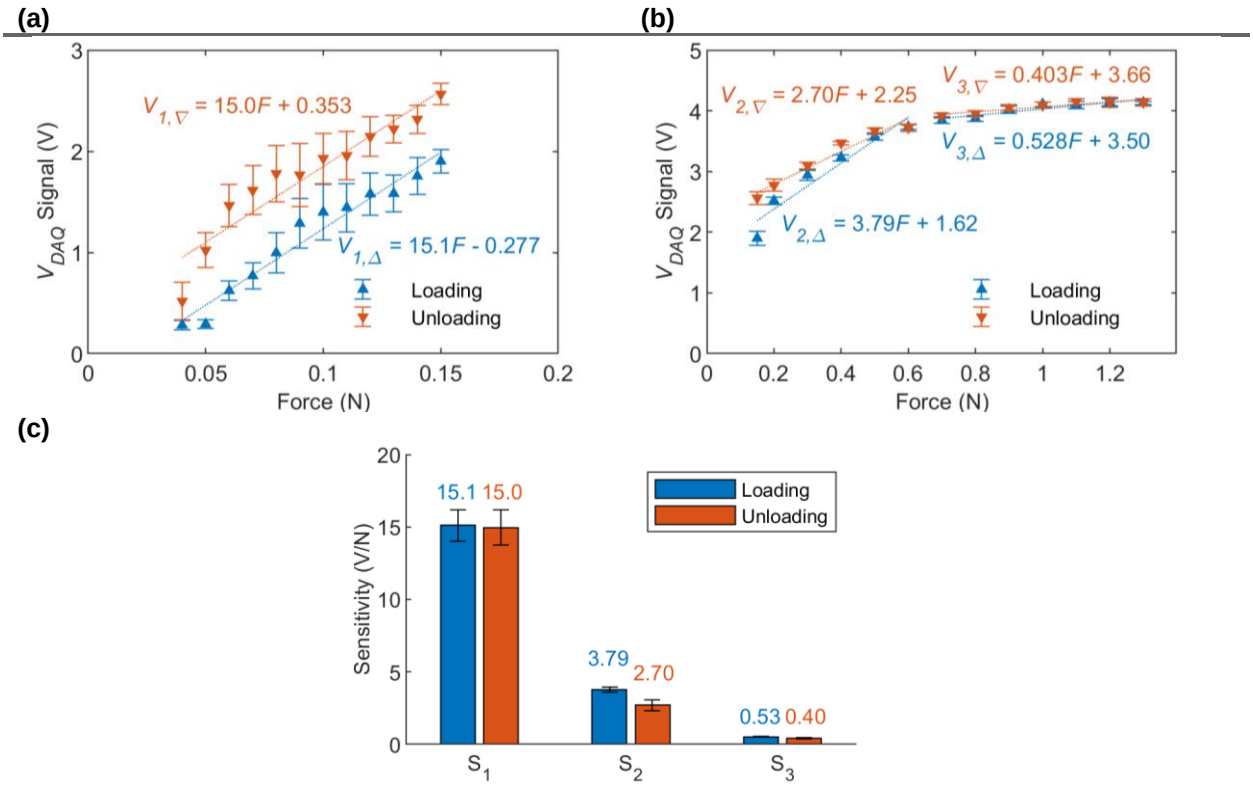


**Figure 10.** (a) Sensor signal-force relationship between 0.04 and 0.15 N forces for loading and unloading for $S_1$, (b) Sensor signal-force relationship between 0.15 and 1.3 N forces for loading and unloading for $S_2$ and $S_3$, (c) Sensitivities for ultra-small force ranges, small force ranges and large force ranges.

Figure 10 (a) and Figure 10 (b) depict the signal-force relationship for the three linear ranges namely $S_1$, $S_2$ and $S_3$ with linear fitting curves and their corresponding characterizing equation. Using the characteristics of the slope of the linear fitting curve, the sensitivities calculated for ultra-small force range ($S_1$: 0.04 – 0.15 N) were 15.1 ± 1.1 V/N and 15.0 ± 1.2 N/V for loading and unloading respectively. The loading and unloading sensitivity for $S_1$ indicated an insignificant difference with a 95% confidence interval ($p = 0.457 > 0.05$). With increasing loading force, the loading sensitivity decreases from 15.1 ± 1.1 V/N to 3.79 ± 0.17 V/N and to 0.528 ± 0.042 V/N. For decreasing unloading forces, the unloading sesnsitivities increases from 0.403 ± 0.045 V/N to 2.70 ± 0.38 V/N and to 15.0 ± 1.2 N/V. Figure 10 (c) outlines the difference between loading and unloading sensitivities for the three distinct linear working ranges of the proposed sensor. The sensitivity difference for loading and unloading for $S_2$ was slightly significant ($p = 0.038 < 0.05$) while that for $S_3$ was significant ($p = 0.003 < 0.05$). The sensitivity of the proposed resistive tactile sensor decreases as the force increases and is directly proportional to the resistance change of the sensor which is in line with characteristics of typical piezoresistive and resistive sensors [27] [40].

As seen from Figure 10 (a), the maximum hysteresis error occurs within the $S_1$ range with largest deviation between loading and unloading of the sensor. The highest hysteresis error occurred for a force of 0.06 N with a value of ± 20%. However, there is significantly less hysteresis error over $S_2$ and $S_3$ (0.15 -1.3 N) linear working ranges which are critical and adequate to monitor and prevent both brain tissue trauma and its complications [5].

D. Accuracy, Resolution and Repeatability

To determine the accuracy of the trimodal signal-force relationship developed from the range and sensitivity analysis, the force measured by the sensor was derived using the characteristics of the linear fitting curves and linear regression [44]. The sensed force was then compared to the reference force subjected to the sensor for a loading frequency of 0.065 N/s for 5 cycles as shown in Figure 11 (a) (ii). For a sample size of 10 resistive tactile sensors, a relative error of 3.47% with a resolution of 0.003 N was calculated. To verify the repeatability, the resistive tactile sensors were subjected to various frequencies for 5 cyclic loadings as shown in Figure 11 (a). The results indicated a repeatability error of 5.10%, 7.75%, 8.72%, 8.56% and 9.53% for 0.013 N/s, 0.065 N/s, 0.13 N/s, 0.2 N/s and 0.26 N/s respectively. It can be concluded that the repeatability error and relative error increases with increasing loading frequency due to equipment limitations and the delay between sensed force and reference force. With a relative error of less than 5%, the sensor indicates good sensor accuracy performance to be used in RMIS application. Furthermore, the sensed force indicated no declination with increasing number of loading and unloading cycles.

E. Stability

The proposed sensor was subjected to a loading frequency of 0.3 N/s for 60 cycles to verify the stability of the printed sensor's signal over surgery time. The results from Figure 11 (b) exhibited stable and consistent signal peaks across all 60 cycles with no degradation with respect to the consistent peak reference forces. Moreover, the sensor demonstrates signal stability even when subjected to minor force variations. This indicates the sensor's ability to accurately detect small forces and deliver reliable and stable signal responses. To meet disposable criteria, the proposed sensor is intended to have a one time use and hence, degradation of the printed material of the sensor after use was not tested.

F. Flexibility and Robustness

Figure 11 (c) depict the proposed sensor in a flexible state. The sensor was subjected to flexural tests to verify its flexibility. Flexibility indicates the sensor's susceptibility to sense small forces applied when in contact with softer materials such as brain tissues during neurosurgeries [29]. Furthermore, being flexible allows the exposed surface of the sensing area of the sensor to flex (bend and deform) accordingly to reaction forces when in contact with tissue during navigation and probing. This enables essential actuation of the sensing device to acquire haptic feedback. Being very flexible also allows the device to be potentially less obstructive during tool-tissue interactions thereby causing less trauma to the patient [45]. The sensor was also subjected to physical crumbling to evaluate the sealing and assembly structural integrity when uncrumpled. The results of the crumpling test (Figure 11 (d)) indicated no alteration to the overall sensor

and, hence, the assembly and its material showed robustness which are critical qualities necessary to ensure the sensor does not detach from its multilayered assembly on the surface of the microgripper surgical tool during use.

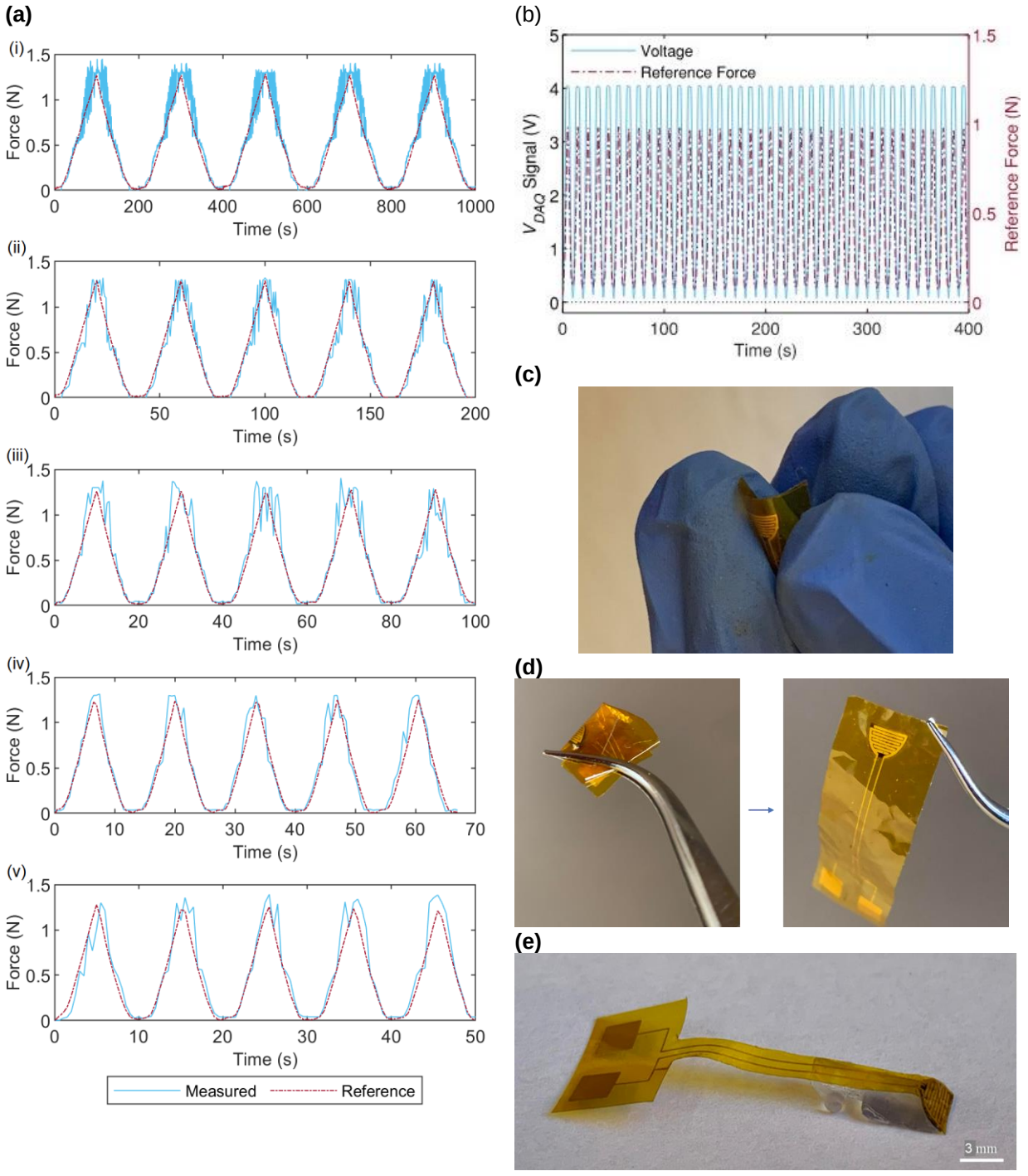


**Figure 11.** (a) Measured sensor response and reference force under different loading frequencies (i) 0.013 N/s, (ii) 0.065 N/s, (iii) 0.13 N/s, (iv) 0.2 N/s and (v) 0.26 N/s, (b) Voltage ($V_{DAQ}$ signal) response and reference force at loading frequency of 0.3 N/s for 60 cycles, (c) Photograph of resistive tactile sensor in bending state (flexural test), (d) Photograph of resistive tactile sensor in crumbled state and uncrumpled state, (e) Photograph of proposed resistive tactile sensor attached to surface of microgripper tip.

Table 1: Summary of Sensor Performance after Optimization for Resistive Tactile Sensors (n = 10)

| Description | Value |
|---|---|
| Minimum Detectable Force | 49.4 ± 6.4 mN |
| Time Response | 70 ± 51 ms |
| Sensitivity<br>$S_1$:<br>0.04 - 0.15 N (Loading)<br>0.04 - 0.15 N (Unloading)<br><br>$S_2$<br>0.15 - 0.6 N (Loading)<br>0.15 - 0.6 N (Unloading)<br><br>$S_3$<br>0.6 - 1.3 N (Loading)<br>0.6 - 1.3 N (Unloading) | <br><br>15.1 ± 1.1 V/N<br>15.0 ± 1.2 V/N<br><br><br>3.79 ± 0.17 V/N<br>2.70 ± 0.38 V/N<br><br><br>0.528 ± 0.042 V/N<br>0.403 ± 0.045 V/N |
| Sensitivity Difference | $S_1$: $p = 0.457 > 0.05$ (Not Significant)<br>$S_2$: $p = 0.038 < 0.05$ (Slightly Significant)<br>$S_3$: $p = 0.003 < 0.05$ (Significant) |
| Average Relative Error | 3.47% for 0.065N/s |
| Resolution | 0.003 N |
| Range | $S_1$: 0.04 - 0.15 N<br>$S_2$: 0.15 - 0.6 N<br>$S_3$: 0.6 - 1.3 N |
| Hysteresis | At 0.06 N (20%) |

## 4. Conclusion

In this study, a screen-printed resistive tactile sensor of 9 $mm^2$ was successfully designed, fabricated, and optimized. The assembled sensor resulted in an ultra-thin sensor design of 110 µm thick with a sensing range of 0.04 - 1.3 N, linear responses, high repeatability, and a low response time (70 ms) while maintaining flexibility and robustness. The screen-printed sensor was comparable to high fabrication cost tactile sensors in terms of performance. Furthermore, the physical geometry of the sensor demonstrated tunable flexibility and, thus, could be adapted to varying surfaces of different surgical tools while meeting the requirements for haptic feedback in RMIS in terms of sensibility range and sensitivity. The proposed resistive tactile sensor can be customized to be mounted onto millimeter-scale surgical tools to increase safety and quality of endoscopic intraventricular surgeries. To demonstrate this capability, in this study, the sensor is customized for the unique surface tip of a magnetically-controlled, 4 mm diameter surgical tool prototype as shown in Figure 11 (e) [4]. The results of the study also suggested that screen printing technologies and advanced material science development could be used in conjunction to develop miniaturized tactile sensors at comparable sensor performance to similar sized sensors developed with complicated and expensive equipment. Screen printing allowed for customized patterns of intricate circuitry and sublayers of multilayered tactile sensors to be fabricated which could possibly advance fabrication processes of disposable miniaturized tactile sensors for RMIS applications in a cost-efficient manner.

In terms of hardware, the conductive tracks and connection pads could be potentially iterated with polyimide sealing, strategic placement, and design within the inside groves of the microgripper for connection to the data acquisition setup and to avoid shorting between the conductive tracks. The sensor and conductive tracks can be coated with a biocompatible polymer composite with shielding properties against electromagnetic interferences [46]. To improve the signal-to-noise ratio of the sensor's output signal, the data-processing module can be optimized by integrating amplifiers with cut-off frequencies. With further advancement, the sensing material could also be directly screen printed onto the surface of the microgripper to reduce the thickness of the sensor and remove attachment hurdles between sensor and tool. For future works, the attached sensor to the microgripper should be calibrated and further optimized for clinical applications for in vitro and cadaver studies. The fabrication, design and findings in this study can be expected to pave the way to building low-cost, sensitive, and disposable biocompatible resistive tactile sensors which would in turn impel the development of robotic minimally invasive surgical tools, increase safety and quality of endoscopic intraventricular surgeries and RMIS.

## 5. Author Information

### Corresponding Author

Hani E. Naguib − Department of Mechanical and Industrial Engineering, University of Toronto, Toronto, Ontario M5S 3G8, Canada; Institute of Biomedical Engineering, University of Toronto, Toronto, Ontario M5S 3G9, Canada; Toronto Rehabilitation Institute, Toronto, Ontario M5G 2A2, Canada; orcid.org/0000-0003-4822-9990; Email: naguib@mie.utoronto.ca

### Authors

D. Anastasia Aubeeluck − Department of Mechanical and Industrial Engineering, University of Toronto, Toronto, Ontario M5S 3G8, Canada

Cameron Forbrigger − Department of Mechanical and Industrial Engineering, University of Toronto, Toronto, Ontario M5S 3G8, Canada

Sara Mohseni Taromsari − Department of Mechanical and Industrial Engineering, University of Toronto, Toronto, Ontario M5S 3G8, Canada

Tianhao Chen − Institute of Biomedical Engineering, University of Toronto, Toronto, Ontario M5S 3G9, Canada

Eric Diller − Department of Mechanical and Industrial Engineering, University of Toronto, Toronto, Ontario M5S 3G8, Canada; University of Toronto Robotics Institute, University of Toronto Engineering, Toronto, Ontario M5S 1A4, Canada

Complete contact information is available at: https://pubs.acs.org/10.1021/acsami.3c04821

### Notes

The authors declare no competing financial interest.

## 6. Acknowledgements

The authors would like to thank the financial support from the Canadian Institutes of Health Research (CIHR) and the Natural Science and Engineering Research Council of Canada (NSERC).

## 7. References

[1] C. Forbrigger, A. Lim, O. Onaizah, S. Salmanipour, T. Looi, J. Drake and E. D. Diller, "Cable-Less, Magnetically Driven Forceps for Minimally Invasive Surgery," *IEEE Robotics and Automation Letters,* vol. 4, no. 2, pp. 1202-1207, 2019.

[2] A. Lim, A. Schonewille, C. Forbrigger, T. Looi, J. Drake and E. Diller, "Design and Comparison of Magnetically-Actuated Dexterous Forceps Instruments for Neuroendoscopy," *IEEE Transactions on Biomedical Engineering,* vol. 68, no. 3, pp. 846-856, 2021.

[3] A. L. Trejos, R. V. Patel and M. D. Naish, "Force sensing and its application in minimally invasive surgery and therapy: A survey," *Proceedings of the Institution of Mechanical Engineers, Part C: Journal of mechanical engineering science,* vol. 224 (7), pp. 1435-1454, 2010.

[4] C. Forbrigger, "Tethered Magnetic Serial Robots for Minimally Invasive," Department of Mechanical and Industrial Engineering, University of Toronto, Toronto, 2023.

[5] H. J. Marcus, K. Zareinia, L. S. Gan, F. W. Yang, S. Lama, G.-Z. Yang and G. R. Sutherland, "Forces exerted during microneurosurgery: a cadaver study," *The international journal of medical robotics + computer assisted surgery,* vol. 10 (2), pp. 251-256, 2014.

[6] L. S. Gan, K. Zareinia, S. Lama, Y. Maddahi, F. W. Yang and G. R. Sutherland, "Quantification of Forces During a Neurosurgical Procedure: A Pilot Study," *World neurosurgery,* vol. 84 (2), pp. 537-548, 2015.

[7] J. S. Ladoiye, D. S. Necsulescu and J. Sasiadek, "Control of Force in Surgical Robots with Random Time Delays Using Model Predictive Control," in *Informatics in Control, Automation and Robotics*, 2019.

[8] P. Puangmali, . K. Althoefer, L. D. Seneviratne, D. Murphy and P. Dasgupta, "State-of-the-Art in Force and Tactile Sensing for Minimally Invasive Surgery," *IEEE Sensor Journal,* vol. 8, no. 4, pp. 371-381, 2008.

[9] M. N. Helmus, D. F. Gibbons and D. Cebon, "Biocompatibility: meeting a key functional requirement of next-generation medical devices," *Toxicologic Pathology,* vol. 36, no. 1, pp. 70-80, 2008.

[10] C. Chi, . X. Sun, N. Xue, T. Li and C. Liu, "Review Recent Progress in Technologies for Tactile Sensors," *Sensors (Basel, Switzerland),* vol. 18 (4), p. 948, 2018.

[11] N. Bandari, J. Dargahi and M. Packirisamy, "Tactile Sensors for Minimally Invasive Surgery: a Review of the State-of-the-art Applications, and Perspectives," *IEEE Access,* vol. 8, pp. 7682-7708, 2020.

[12] J. Kim, R. Kumar, A. J. Bandodkar and J. Wang, "Advanced Materials for Printed Wearable Electrochemical Devices: A Review," *Advanced electronic materials,* vol. 3 (1), pp. 1600260-n/a, 2017.

[13] Y. Zhang, Y. Zhu, S. Zheng, L. Zhang, X. Shi, J. He, X. Chou and Z.-S. Wu, "Ink formulation, scalable applications and challenging perspectives of screen printing for emerging printed microelectronics," *Journal of energy chemistry,* vol. 63, pp. 498-513, 2021.

[14] A. Pourghodrat and C. A. Nelson, "Disposable Fluidic Actuators for Miniature In-Vivo Surgical Robotics," *Journal of medical devices,* vol. 11 (1), pp. 0110031-0110038, 2017.

[15] Y. Zhu, Y. Liu, Y. Sun, Y. Zhang and G. Ding, "Recent Advances in Resistive Sensor Technology for Tactile Perception: A Review," *IEEE sensors journal,* vol. 22 (16), pp. 15635-15649, 2022.

[16] J. Li, L. Fang, B. Sun, X. Li and S. H. Kang, "Review—Recent Progress in Flexible and Stretchable Piezoresistive Sensors and Their Applications," *Journal of The Electrochemical Society,* vol. 167, no. 3, p. 037561, 2020.

[17] F. Aviles, A. I. Oliva-Aviles and M. Cen-Puc, "Piezoresistivity, Strain, and Damage Self-Sensing of Polymer Composites Filled with Carbon Nanostructures," *Advanced engineering materials,* vol. 20, no. 7, p. 1701159, 2018.

[18] Y. Peng, N. Yang, Q. Xu, Y. Dai and Z. Wang, "Recent Advances in Flexible Tactile Sensors for Intelligent Systems," *Sensors (Basel, Switzerland),* vol. 21 (16), p. 5392, 2021.

[19] S. Khan, L. Lorenzelli and R. S. Dahiya, "Technologies for Printing Sensors and Electronics Over Large Flexible Substrates: A Review," *IEEE sensors journal,* vol. 15 (6), pp. 3164-3185, 2015.

[20] L. Gan, M. Dong, Y. Han, Y. Xiao, L. Yang and J. Huang, "Connection-Improved Conductive Network of Carbon Nanotubes in a Rubber Cross-Link Network," *ACS applied materials & interfaces,* vol. 10 (21), pp. 18213-18219, 2018.

[21] D. Li, T. Zhai, Q. Gong, G. Fei and H. Xia, "Effect of processing temperature on structure and properties of microinjection moulded thermoplastic polyurethane/multiwalled carbon nanotube composites," *Plastics, rubber & composite,* vol. 44 (5), pp. 197-205, 2015.

[22] H. Le Trong, K. Kiryukhina, M. Gougeon, V. Baco-Carles, F. Courtade, S. Dareys and P. Tailhades, "Paramagnetic behaviour of silver nanoparticles generated by decomposition of silver oxalate," *Solid state sciences,* vol. 69, pp. 44-49, 2017.

[23] S. D. Ramôa, G. M. Barra, R. V. Oliveira, M. G. de Oliveira, M. Cossa and B. G. Soares, "Electrical, rheological and electromagnetic interference shielding properties of thermoplastic polyurethane/carbon nanotube composites: Electromagnetic shielding properties of TPU/CNT composites," *Polymer international,* vol. 62 (10), pp. 1477-1484, 2013.

[24] S. Lee, T. Yoo, Y. Han, H. Kim and H. Han, "Polyimide–Epoxy Composites with Superior Bendable Properties for Application in Flexible Electronics," *Journal of electronic materials,* vol. 46 (8), pp. 4740-4749, 2017.

[25] G. J. Donley, W. W. Hyde, S. A. Rogers and F. Nettesheim, "Yielding and recovery of conductive pastes for screen printing," *Rheologica acta,* Vols. 58 (6-7), pp. 361-382, 2019.

[26] T. Chen, Z. Saadatnia, J. Kim, T. Looi, J. Drake, E. Diller and H. E. Naguib, "Novel, Flexible, and Ultrathin Pressure Feedback Sensor for Miniaturized Intraventricular Neurosurgery Robotic Tools," *IEEE Transactions on Industrial Electronics,* vol. 68, no. 5, pp. 4415-4425, 2021.

[27] Y. Gao, J. Feng, F. Liu and Z. Liu, "Effects of Organic Vehicle on the Rheological and Screen-Printing Characteristics of Silver Paste for LTCC Thick Film Electrodes," *Materials 2022,* vol. 15(5), p. 1953, 2022.

[28] H.-W. Lin, C.-P. Chang, W.-H. Hwu and M.-D. Ger, "The rheological behaviors of screen-printing pastes," *Journal of materials processing technology,* vol. 197 (1), pp. 284-291, 2008.

[29] A. Tejo-Otero, F. Fenollosa-Artés, I. Achaerandio, S. Rey-Vinolas, I. Buj-Corral, M. Á. Mateos-Timoneda and E. Engel, "Soft-Tissue-Mimicking Using Hydrogels for the Development of Phantoms," *Gels,* vol. 8 (1), p. 40, 2022.

[30] M. Navarro-Lozoya, M. S. Kennedy, D. Dean and J. I. Rodriguez-Devora, "Development of phantom material that resembles compression properties of human brain tissue for training models," *Materialia,* vol. 8, p. 100438, 2019.

[31] Y. Zhang, G. Shi, J. Qin, S. E. Lowe, S. Zhang, H. Zhao and Y. L. Zhong, "Recent Progress of Direct Ink Writing of Electronic Components for Advanced Wearable Devices," *ACS applied electronic materials,* vol. 1 (9), pp. 1718-1734, 2019.

[32] M. Amirkhosravi, L. Yue and I. Manas-Zloczower, "Dusting Thermoplastic Polyurethane Granules with Carbon Nanotubes toward Highly Stretchable Conductive Elastomer Composites," *ACS applied polymer materials,* vol. 2 (9), pp. 4037-4044, 2020.

[33] H.-J. Choi, M. S. Kim, D. Ahn, S. Y. Yeo and S. Lee, "Electrical percolation threshold of carbon black in a polymer matrix and its application to antistatic fibre," *Scientific Reports,* vol. 9 (1), pp. 6338-6338, 2019.

[34] F. Stan, R. T. Rosculet and C. Fetecau, "Direct Current method with reversal polarity for electrical conductivity measurement of TPU/MWCNT composites," *Measurement : Journal of the International Measurement Confederation,* vol. 136, pp. 345-355, 2019.

[35] F. Jiang, L. Zhang, Y. Jiang, Y. Lu and W. Wang, "Effect of annealing treatment on the structure and properties of polyurethane/multiwalled carbon nanotube nanocomposites," *Journal of applied polymer science,* vol. 126 (3), pp. 845-85, 2012.

[36] L. Gao, C. Zhu, L. Li, C. Zhang, J. Liu, H.-D. Yu and W. Huang, "All Paper-Based Flexible and Wearable Piezoresistive Pressure Sensor," *ACS applied materials & interfaces,* vol. 11 (28), pp. 25034-25042, 2019.

[37] L. Paredes-Madrid, A. Matute, J. Bareño, C. P. V. Vargas and E. Gutierrez, "Underlying Physics of Conductive Polymer Composites and Force Sensing Resistors (FSRs). A Study on Creep Response and Dynamic Loading," *Materials,* vol. 10, no. 11, p. 1334, Nov. 2017.

[38] N. Ibrahim, J. O. Akindoyo and M. Mariatti, "Recent development in silver-based ink for flexible electronics," *Journal of science. Advanced materials and devices,* vol. 7 (1), p. 100395, 2022.

[39] M. Aggravi, E. De Momi, F. DiMeco, F. Cardinale, G. Casaceli, M. Riva, G. Ferrigno and D. Prattichizzo, "Hand–tool–tissue interaction forces in neurosurgery for haptic rendering," *Medical & biological engineering & computing,* vol. 54 (8), pp. 1229-1241, 2016.

[40] C. Xie, M. Zhang, W. Du, C. Zhou, Y. Xiao, S. Zhang and M. Chan, "Sensing-range-tunable pressure sensors realized by self-patterned-spacer design and vertical CNT arrays embedded in PDMS," *RSC advances,* vol. 1 (55), pp. 33558-33565, 2020.

[41] L. Zou, C. Ge, Z. J. Wang, E. Cretu and X. Li, "Novel Tactile Sensor Technology and Smart Tactile Sensing Systems: A Review," *Sensors (Basel, Switzerland),* vol. 17 (11), p. 265, 2017.

[42] W. Cheng, J. Wang, Z. Ma, K. Yan, Y. Wang, H. Wang, S. Li, Y. Li, L. Pan and Y. Shi, "Flexible Pressure Sensor With High Sensitivity and Low Hysteresis Based on a Hierarchically Microstructured Electrode," *IEEE electron device letters,* vol. 39 (2), pp. 288-291, 2018.

[43] S. Pyo, J. Lee, K. Bae, S. Sim and J. Kim, "Recent Progress in Flexible Tactile Sensors for Human-Interactive Systems: From Sensors to Advanced Applications," *Advanced materials (Weinheim),* vol. 33 (47), pp. e2005902-n/a, 2021.

[44] L. Wang, T. Ding and P. Wang, "Thin Flexible Pressure Sensor Array Based on Carbon Black/Silicone Rubber Nanocomposite," *IEEE sensors journal,* vol. 9 (9), pp. 1130-1135, 2009.

[45] S. Sokhanvar, J. Dargahi, S. Najarian and S. Arbatani, "Tactile Sensing and Displays haptic feedback for minimally invasive surgery and robotics," in *Haptic Feedback for Minimally Invasive Surgery and Robotics*, United Kingdom, John Wiley & Sons, 2013, pp. 98-111.

[46] Z. Ameri, E. Soleimani and A. Shafyei, "Preparation and identification of a biocompatible polymer composite: Shielding against the interference of electromagnetic waves," *Synthetic metals,* vol. 283, p. 116983, 2022.